A model of actin-driven endocytosis explains differences of endocytic motility in budding and fission yeast

Masoud Nickaeen[a], Julien Berro[c,d], Thomas D. Pollard[b,c], and Boris M. Slepchenko[a,*]
[a]Richard D. Berlin Center for Cell Analysis and Modeling, Department of Cell Biology, University of Connecticut Health Center, Farmington, CT 06030; [b]Department of Molecular Cellular and Developmental Biology, Yale University, [c]Department of Molecular Biophysics and Biochemistry, Yale University, and Department of Cell Biology, Yale University School of Medicine, New Haven, CT 06511, and [d]Nanobiology Institute, Yale University, New Haven, CT 06520

ABSTRACT **A comparative study (Sun *et al.*, 2019) showed that the abundance of proteins at sites of endocytosis in fission and budding yeast is more similar in the two species than previously thought, yet membrane invaginations in fission yeast elongate twofold faster and are nearly twice as long as in budding yeast. Here we use a three-dimensional model of a motile endocytic invagination (Nickaeen *et al.*, 2019) to investigate factors affecting elongation of the invaginations. We found that differences in turgor pressure in the two yeast species can largely explain the paradoxical differences observed experimentally in endocytic motility.**

Monitoring Editor
Alex Mogilner
New York University

Received: Jul 20, 2021
Revised: Nov 23, 2021
Accepted: Dec 10, 2021

INTRODUCTION

As in plant cells, endocytosis in yeast cells occurs under high turgor pressure estimated to be ~10 atm in fission yeast (Basu *et al.*, 2014; Lacy *et al.*, 2018) and about a fifth to half of that in budding yeast (de Maranon *et al.*, 1996; Schaber *et al.*, 2010). Transient assembly of small, dense networks of actin filaments at endocytic sites (termed "actin patches") is necessary for robust endocytosis in yeast (Aghamohammadzadeh and Ayscough, 2009; Basu *et al.*, 2014), suggesting that assembly of an actin patch around a nascent invagination of the plasma membrane may generate a pulling force sufficient to elongate the invagination under such pressures. Many studies have investigated the mechanisms of force generation at endocytic sites in yeast (Carlsson and Bayly, 2014; Scher-Zagier and Carlsson, 2016; Carlsson, 2018; Kaksonen and Roux, 2018; Lacy *et al.*, 2018; Mund *et al.*, 2018; Nickaeen *et al.*, 2019).

A comparative study of endocytosis in fission and budding yeast (Sun *et al.*, 2019) found that with the exception of twofold more polymerized actin in fission yeast the abundances of proteins participating in patch assembly are more similar than previously thought. Nevertheless, elongation of an endocytic invagination is twofold faster (~52 nm/s) in fission yeast than in budding yeast (~24 nm/s). The fast elongation rates in both yeasts indicate that driving forces generated at endocytic sites substantially overpower resistance from turgor pressure, not just withstand it.

For the turgor pressure of 10 atm, a rough estimation of a resisting force acting on a cylindrical tubule with a typical radius of ~30 nm yields ~3000 pN (Carlsson, 2018; Lacy *et al.*, 2018). Simulations based on a spatial model of a motile invagination proposed by Nickaeen *et al.* (2019) showed that an actin patch assembling around such a tubule can generate tangential pulling forces of ~2500 pN that can withstand a turgor pressure of ~9 atm. For lower turgor pressures, the tubule would elongate, albeit slowly, for example, at only ~2 nm/s against a turgor pressure of ~7 atm.

Yet the simulations of the model made another prediction that the assembling patch would also generate normal forces, which squeeze the tubule at its base and stretch it at its middle, thus transforming the invagination shape from cylindrical to flasklike (or "head–neck") as observed in electron micrographs of budding yeast (Kukulski *et al.*, 2012; Buser and Drubin, 2013). Previous modeling studies also predicted endocytic invaginations with head–neck shapes (Dmitrieff and Nédélec, 2015; Ma and Berro, 2021). Since the resisting force is the product of turgor pressure and the cross-sectional area at the base of the invagination, the transition to the

This article was published online ahead of print in MBoC in Press (http://www.molbiolcell.org/cgi/doi/10.1091/mbc.E21-07-0362) on December 15, 2021.
*Address correspondence to: Boris M. Slepchenko (boris@uchc.edu).
Abbreviation used: NPFs, nucleation promoting factors.

head–neck shape may dramatically reduce resistance due to turgor pressure, leading to faster elongation rates even for turgor pressures of ~10 atm.

Our previous study, as well as works of others (Carlsson and Bayly, 2014; Mund *et al.*, 2018), modeled the invaginations as spherocylinders. In those simulations, we approximated the reduction in resistance due to the putative shape change by replacing fixed resistance with a resistance decreasing over time. The elongation rate increased fourfold, to ~8 nm/s, which is still significantly lower than the 25–50 nm/s range reported by Sun *et al.*, (2019).

In this study, we solved our model in geometries mimicking flasklike invaginations. The solutions yielded higher driving forces, because, in contrast with cylindrical shapes for which pulling forces are viscous in nature, active stresses also contribute to the forces driving flasklike invaginations. Consistent with the experimental data (Sun *et al.*, 2019), invagination is faster and deeper at high turgor pressures, because at higher initial resistance, more actin filaments accumulate by the time the driving force overcomes the resistance, producing higher driving forces during elongation.

RESULTS

Model

Our model, described in detail in Nickaeen *et al.* (2019), couples kinetics of actin nucleation, polymerization, and turnover constrained by counts of each participating protein over time (Berro *et al.*, 2010), with the mechanics of the assembling filamentous meshwork approximated as that of a visco-active gel (Kruse *et al.* 2005; Prost *et al.*, 2015). Mathematically, the model consists of advection-reaction equations governing densities of proteins involved in patch assembly (see Eq (S1) in the Supplemental Material), and a force-balance equation yielding actin velocities [Eq (S2) of the Supplemental Material]. In the advection-reaction equations, reaction rates and rate constants from the experimental literature (Berro *et al.*, 2010; see also Supplemental Table S1 in the Supplemental Material) were modified to reflect effects of forces and filament densities on polymerization kinetics. The equation, which governs actin flow, balances active forces, originating from impingement of polymerized subunits on existing filaments, with viscous forces that arise due to entanglement and cross-linking of branched filaments. The active and viscous forces derive, respectively, from repulsive and viscous stresses in the meshwork of overlapping actin filaments, which are both proportional to the square of local density of polymerized subunits; the viscous stresses are also proportional to the local average of filament lengths [Gardel *et al.*, 2003; Nickaeen *et al.*, 2019; see also Eq (S3) in the Supplemental Material]. The coefficients determining scales of the stresses were inferred from rheological properties of actin filament networks (Mullins *et al.*, 1998; Gardel *et al.*, 2003; Tseng and Wirtz, 2004).

Through interactions with the membrane, the flow of polymerized actin exerts on the invagination driving forces parallel to its axis. The resultant driving force (f_{drive}) and resistance due to turgor pressure (f_{resist}) are the factors determining elongation rate in our model. We ignore small resistive forces due to membrane surface tension. We also assume sufficient supply of lipids by way of exocytosis and lateral diffusion and impose no constraint on total area of the invaginated membrane.

To determine the time-dependent driving force $f_{\text{drive}}(t)$, we integrate over the surface of the invagination, for each t, the active and viscous forces exerted on the invagination by actin flow and then project the resultant force on the invagination axis [see Supplemental Material, Eq (S4)].

As mentioned in the *Introduction*, the resistive force can also depend on time, even at a fixed turgor pressure. Indeed, our previous study revealed that an assembling actin patch produces not only a pulling force but also generates orthogonal forces that squeeze the base of the invagination and stretch its middle (Figure 1A). As actin filaments accumulate around a nascent spherocylindrical invagination, squeezing forces at the base of the invagination can reach the magnitude amounting to additional pressure of ~8.5 atm (Figure 1B). It is therefore likely that at some point during patch assembly, the nascent invaginations, such as the one shown in Figure 1A, acquire head–neck shapes (Figure 1C). Such shapes were observed in electron micrographs of invaginations in budding yeast (Kukulski *et al.*, 2012; Buser and Drubin, 2013) and predicted theoretically for a membrane elongated under high turgor pressure by a point force exerted at its tip (Dmitrieff and Nédélec, 2015; Ma and Berro, 2021). Because turgor pressure is isotropic and thus pushes on the upper surface of the head of the invagination as well, the transition from cylindrical shape to flasklike shape, such as in Figure 1C, results in $f_{\text{resist}}(t)$ decreasing with time (Figure 1D). We specify this function later in this subsection (see also Figure 1D, Eq (2) below, and Nickaeen *et al.* (2019)].

Solving for dynamics of the invagination shape would involve mechanics of a moving membrane (Powers, 2010) and require

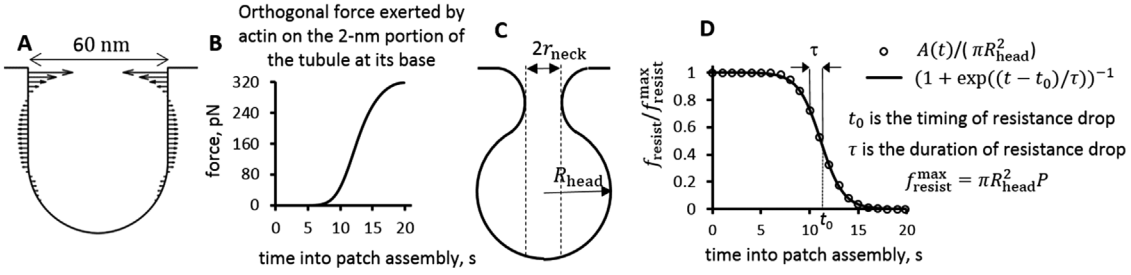

FIGURE 1: An assembling endocytic actin patch exerts strong squeezing forces at its base of an initial invagination. (A) Example of distribution of orthogonal forces in an (*r, z*)-section of a nascent invagination adapted from simulation results in Figure 5A of Nickaeen *et al.* (2019). (B) Time dependence of squeezing force acting on the 2 nm wide portion at the base of the nascent tubule in (A), from a simulation described in Figure 5A of Nickaeen *et al.* (2019). The force of 320 pN applied to a 2 nm-wide band with the radius of 30 nm amounts to additional pressure of ≈ 8.5 atm. (C) Cartoon of a head–neck (flasklike) shape with radii r_{neck} and R_{head}; since turgor pressure P is isotropic, f_{resist} for this shape diminishes to $\pi r_{neck}^2 P$. (D) Graph of $f_{\text{resist}}(t)$ normalized to $f_{resist}^{max} = \pi R_{head}^2 P$ [dots, $A(t)$ is the cross-action area at the base, see the text] is well approximated by function $\{1 + \exp[(t - t_0)/\tau]\}^{-1}$ (solid curve) with the fitted timing (t_0) and duration (τ) of the resistance decrease caused by shape change.

reliable experimental data describing rheological characteristics of both the membrane and its protein coat. Lacking this information, we initialize invaginations as already having head–neck shapes with specified head and neck radii R_{head} and r_{neck}, which do not change as the neck elongates. As in Nickaeen *et al.* (2019), we assume that all points of the membrane move with the same speed $u(t)$ described by a linear force-velocity relation,

$$u(t) = \mu \cdot \left[f_{drive}(t) - f_{resist}(t) \right] \quad (1)$$

where μ is the invagination mobility coefficient. The inverse of the mobility, representing "resistivity" of the invagination with respect to a net driving force, is likely determined by viscosity of the membrane and its protein coat, including links to actin filaments. Our model is only modestly sensitive to μ (see *The head–neck invaginations elongate faster and to greater depths under higher turgor pressures*), so this parameter is not critical for explaining the twofold differences in elongation rates and depths reported in Sun *et al.* (2019). Note that for the invagination to elongate, the driving force must exceed the resistance of turgor pressure; therefore, Eq. (1) holds only for $f_{drive}(t) \geq f_{resist}(t)$, whereas for $f_{drive}(t) < f_{resist}(t), u(t) = 0$.

Because the resistance of turgor pressure is proportional to the invagination cross-section area near its base (Nickaeen *et al.*, 2019), we can gain insight into general behavior of $f_{resist}(t)$ by estimating the time dependence of this area, $A(t)$, for the example illustrated by Figure 1A. To compute the resistive force normalized to its maximum, $f_{resist}(t) / f_{resist}^{max} = A(t) / \left(\pi R_{head}^2 \right)$, where $f_{resist}^{max} = \pi R_{head}^2 P$ and P is the turgor pressure, we assumed Hookean elasticity of the protein coat for this case (i.e., that the diameter of the opening decreases in proportion to the squeezing force shown in Figure 1B) with such stiffness that the opening would close when the squeezing force reached its maximum. Notably, the results (dotted curve in Figure 1D) are accurately fitted by the function $\left\{ 1 + \exp\left[(t - t_0)/\tau \right] \right\}^{-1}$ with suitable timing t_0 and duration τ of the resistance descent (solid curve in Figure 1D with $t_0 \approx 11.1$ s and $\tau \approx 1.2$ s). While the assumptions made above may be simplistic (e.g., the coat elasticity may not be Hookean), the formulation of $f_{resist}(t)$ in terms of the timing and duration of the resistance drop is fairly general. We therefore approximate the resistive force in this study by the following function of time,

$$f_{resist}(t) = \frac{\pi R_{head}^2 P}{1 + e^{\frac{t - t_0}{\tau}}} \quad (2)$$

and treat t_0 and τ as model parameters [see also Eq (2*) in *The head–neck invaginations elongate faster and to greater depths under higher turgor pressures*]. Note that because the reduction of resistance occurs due to the shape change, t_0 in our model also represents the time around which the transition to a head–neck shape takes place.

Nucleation-promoting factors (NPFs)—the proteins that stimulate Arp2/3 complex to nucleate branched actin filaments—reside on the invaginating membrane where they concentrate in narrow rings around the membrane. Fission yeast has two rings of NPFs, one that remains in the initial position at the base of the invagination at the plasma membrane and the other that moves with the tip of the tubule (Arasada and Pollard, 2011; Arasada *et al.*, 2018), whereas budding yeast has one ring of NPFs that remains near the base of the invagination (Mund *et al.*, 2018). As with cylindrical shapes (Nickaeen *et al.*, 2019), simulations of both arrangements of NPFs on head–neck surfaces yielded similar elongation rates and tip displacements. To avoid duplication, we employ the two-zone arrangement of NPFs characteristic of fission yeast to illustrate our findings throughout this paper.

In summary, we assume that a nascent endocytic invagination begins to elongate when the driving force exerted on it by the assembling actin patch overcomes resistance of turgor pressure, and that the elongation rate is proportional to the difference of the two forces [(Eq (1)]. Dynamics of the driving force depend on mechanical stresses developing in the patch. Thus the driving force is ultimately determined by the nucleation and polymerization kinetics of actin and by the flow of actin filaments. The latter is governed by local force balance in the patch subjected to a no-slip condition at the interface with the invaginated membrane. Given that the invagination shape likely transforms in the process from cylindrical to flasklike, we further assume that the turgor resistance decreases with time [Eq (2)]. A mathematical description of the model and its numerical solution are detailed in the Supplemental Material [Eqs (S1)–(S4)] and in Nickaeen *et al.* (2019). Because the invaginations in our model are axially symmetric, we compute and present actin densities in (r, z) coordinates (see *Methods*).

Changing the shape of the invagination from cylindrical to flasklike amplifies driving forces, yielding faster elongation and longer displacements

If only the reduction of resistance, described by Eq (2), is taken into account, cylindrical invaginations did not elongate as fast as observed experimentally (see *Introduction*). Seeking faster elongations, we noted that the shape change should also affect the driving force. Indeed, driving forces originate from stresses in the actin filament meshwork surrounding the invagination, and while the forces pulling cylindrical invaginations derive from viscous stresses, the driving forces exerted on curved invaginations would have additional contributions from active stresses due to the actin flow pushing on the upper surface of the invagination head. This would not only increase the driving force during elongation but might also make elongation rates more sensitive to the invagination mobility coefficient μ [Eq (1)].

The elongation rates of cylindrical invaginations are essentially insensitive to μ because the viscous driving forces depend on shear rates of actin flow at the invagination that are lower for invaginations with higher mobility (see the black and gray dashed curves in Figure 3, A and B discussed later in this section). As a result, the increase of μ is counterbalanced by the drop in the viscous pulling force, leaving the elongation rate $u(t)$ virtually unchanged (Nickaeen *et al.*, 2019). In contrast, the forces driving a flasklike invagination might be less sensitive to reductions in shear rates. The reason is that active stresses are by definition independent of shear rates and so are their contributions to the driving force.

We tested these hypotheses by solving the model in geometries mimicking invaginations with head–neck shapes. To maximize elongation rates, we explored shapes with small ratios r_{neck}/R_{head} (the head radius was fixed at 30 nm). Given the reported similarity of protein abundances in fission and budding yeast, we ran all simulations with the same set of reaction rate constants and abundances of soluble proteins taken from Berro *et al.* (2010) and Nickaeen *et al.* (2019). Similarly, we uniformly applied coefficients setting the scales for active and viscous stresses as they were derived in our previous study. Results were consistent with our expectations, as exemplified by a solution obtained for an invagination with $r_{neck}/R_{head} = 0.1$ (Figure 2) using the same parameters as for the cylindrical invagination in our

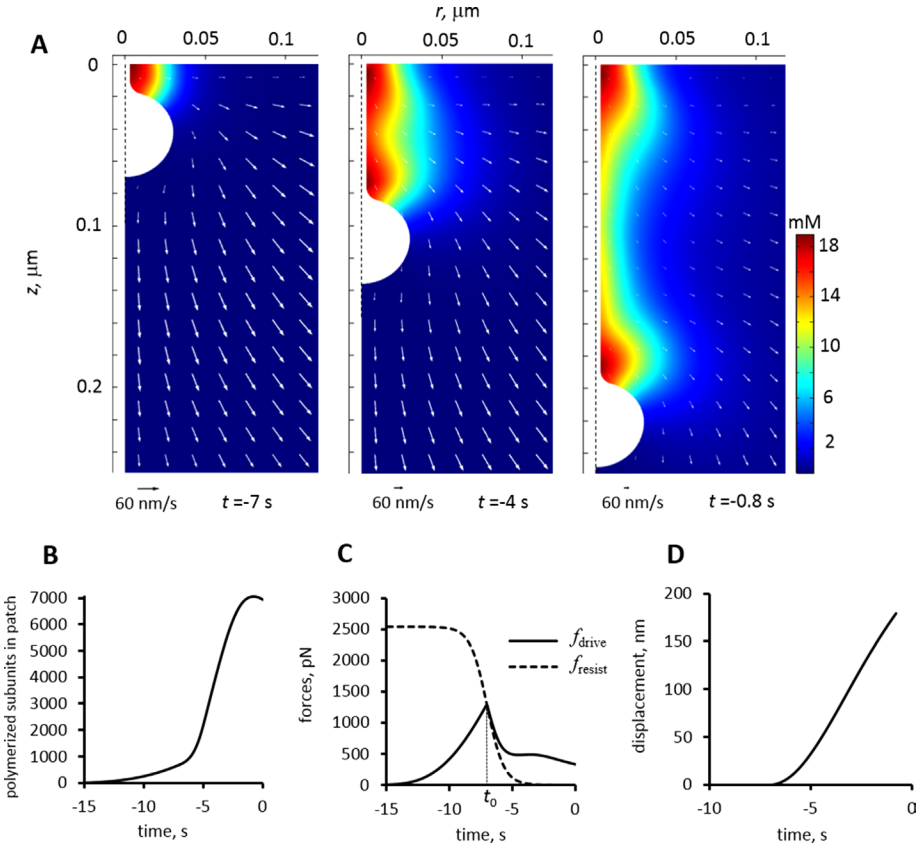

FIGURE 2: Modeling an elongating invagination with head–neck shape. We simulated elongation of the head–neck invagination described by $r_{neck}/R_{head} = 0.1$ using the following parameters: $P = 9$ atm, $t_0 = -7$ s (13 s into patch assembly), $\tau = 0.66$ s, and $\mu = 0.08$ nm/s/pN. Similar to experimental studies, the time here and below is offset by –20 s so that the times of actin peaks would be around time zero. (A) The (*r*, *z*) sections of 3D distributions of actin densities (pseudocolors) and velocities (white arrows) are shown for three times: (left) beginning of elongation, (middle) actin half maximum, and (right) actin peak. Extracellular space is white; vertical dashed lines represent the axis of symmetry of model geometry. Velocity scale bars correspond to 60 nm/s. (B) Polymerized actin as a function of time. The numbers of subunits were counted inside a growing cylinder embedding the moving invagination: $r_{cyl} = 0.06$ μm, $z_{cyl} = l + \delta l + \int_{t_{begin}}^{t} u(t')dt'$, where t_{begin} denotes the beginning of elongation and lengths are in μm: the initial invagination length $l = 0.07$ μm and short extra length $\delta l = 0.003$ μm. (C) Time dependence of driving force (solid curve) and resistance due to turgor pressure described by Eq (2) (dashed curve); the invagination mobility used is $\mu = 0.08$ μm/s/pN. (D) Displacement is ~180 nm at the time actin peaks, which is thought to coincide with scission, yielding average elongation rate ~30 nm/s over the duration of elongation, $t_{scission} - t_{begin}$.

previous study (Figure 7 in Nickaeen *et al.*, 2019), with the exception of the mobility coefficient value $\mu = 0.08$ nm/(s·pN), which is twice the one used for the cylindrical invagination[1].

The snapshots of the (*r*, *z*) sections in Figure 2A correspond to the beginning of elongation (left), actin half-maximum (middle), and actin peak (right). The times in this figure and below are offset by –20 s so that on the transformed scale, actin peaks, which are thought to coincide with the scission of the endocytic vesicle (Sun *et al.*, 2019), occur around time zero (Figure 2B). Thus the offset readings are close to times before scission.

A nascent invagination begins to elongate (Figure 2D) at the time t_{begin} when the solid curve in Figure 2C, depicting the driving force, intersects with the dashed graph of the resistance of turgor pressure.

[1]All simulations in our previous study were run with μ = 0.04 nm/(s·pN), not μ = 0.4 nm/(s·pN) as misstated in Nickaeen *et al.* (2019). The typographical error had no effect on the results of Nickaeen *et al.* (2019).

In this particular example, t_{begin} coincides with t_0, but generally may deviate from it, as discussed in the next section. The driving force, rising at $t < t_{begin}$, starts "shadowing" the descending $f_{resist}(t)$ immediately after t_{begin} (Figure 2C). This transition is largely a result of an abrupt drop of the viscous component of f_{drive} caused by the decrease in the shear rate, as the moving invagination catches up with the surrounding actin flow.

Assuming the vesicle scission coincides with the time of maximum actin, the simulated duration of elongation is 6.2 s. Notably, the maximum displacement 179 nm (Figure 2D) yielded by the model is within the range of displacements measured in yeast: ~125 nm in budding yeast and ~200 nm in fission yeast (Sun *et al.*, 2019). The average elongation rate is then 179 nm/6.2 s = 28.9 nm/s. The maximum elongation rate, achieved at $t = -3.3$ s, is 38 nm/s. Both the average and the maximum values are in the range of speeds reported by Sun *et al.* (2019). Thus, solving the model in geometries mimicking curved flasklike invaginations and with the amplified invagination mobility produced elongation rates and displacements comparable with experimental data.

The factors contributing to the greater speeds and displacements can be elucidated further by comparing simulations that differ only by invagination shape and mobility. For this, we reran the simulation described above with $\mu = 0.04$ nm/(s·pN) and compared results of both simulations with the solutions of the same model for the cylindrical invagination with $\mu = 0.04$ nm/(s·pN) from our previous study and for the cylindrical invagination with $\mu = 0.08$ nm/(s·pN) (Figure 3).

Changing the shape from cylindrical to flasklike produced a threefold higher maximum of the net driving force, $f_{net}(t) = f_{drive}(t) - f_{resist}(t)$ (dotted and black dashed curves in Figure 3A).

Because all four solutions were obtained with the same $f_{resist}(t)$, the higher f_{net} reflects the anticipated increase of f_{drive}. Note that both head-neck and cylindrical invaginations with higher mobility experience lower f_{net} (dotted vs. solid and black vs. gray dashed curves in Figure 3A) because the contributions of viscous stresses to f_{drive} depend on shear rates, which are lower for higher μ, as discussed above. Yet overall, the elongation rates $u(t) = \mu f_{net}(t)$ are noticeably faster for the head–neck invagination with the higher μ (solid and dotted curves in Figure 3B), which validates the prediction that the elongation of curved invaginations is more sensitive to μ than that of the cylindrical invaginations (dashed curves in Figure 3, B and C). The maximum elongation rates in Figure 3B were as follows: (solid curve) 38.0 nm/s, (dotted curve) 31.2 nm/s, (black dashed curve) 9.9 nm/s, and (gray dashed curve) 10.5 nm/s. Higher elongation rates translate into larger maximal dispacements $\Delta z_{tip} = \int_{t_{begin}}^{t_{scission}} u(t')dt'$, where $t_{scission}$ is intepreted as the time of the peak of actin (Figure 3C). The Figure 3 legend gives the values of t_{begin} and $t_{scission}$ for each of

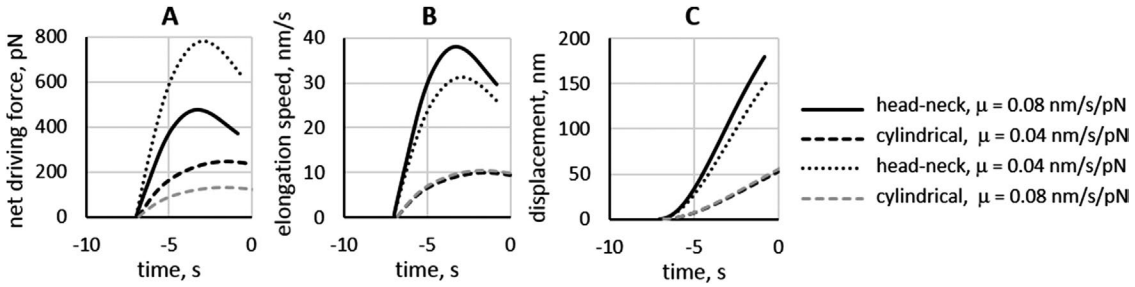

FIGURE 3: Invaginations with "head–neck" shape have higher driving forces than cylindrical invaginations, yielding faster elongation and longer displacements. Dependence of (A) net driving force, $f_{net} = f_{drive} - f_{resist}$, (B) elongation rates, and (C) displacements on the invagination geometry and μ. The model was solved with the same parameters (with the exception of invagination mobility) for the invagination with head–neck shape ($r_{neck}/R_{head} = 0.1$) and mobility coefficients $\mu = 0.08$ μm/s/pN (solid curves) and 0.04 μm/s/pN (dotted curves) and for the cylindrical invagination with $\mu = 0.08$ μm/s/pN (gray dashed curves) and 0.04 μm/s/pN (black dashed curves). The head–neck invaginations began to move at $t_{begin} = -7$ s, and the cylindrical invaginations started to elongate at $t_{begin} = -6.8$ s. Vesicle scission, terminating elongation, is thought to occur when polymerized actin reaches its maximum. For the head–neck invaginations, $t_{scission} = -0.8$ s for $\mu = 0.08$ μm/s/pN and –0.6 s for $\mu = 0.04$ μm/s/pN, and for the cylindrical invaginations, $t_{scission} = 0$ s for $\mu = 0.04$ μm/s/pN and 0.9 s for $\mu = 0.08$ μm/s/pN. The displacements at $t_{scission}$ were 179 nm (solid curve), 153 nm (dotted curve), 64 nm (gray dashed curve), and 52 nm (black dashed curve).

the solutions. Based on these data, the average elongation rates $\overline{u} = \Delta z / \left(t_{scission} - t_{begin}\right)$ are (solid curve) 28.9 nm/s, (dotted curve) 23.9 nm/s, (black dashed curve) 7.7 nm/s, and (gray dashed curve) 8.3 nm/s.

In this study, we do not explicitly model the transition of a nascent cylindrical invagination into a flask shape. Instead, initial invaginations in our simulations are already of a head–neck shape, with R_{head} and r_{neck} that the invagination would assume as a result of shape change. Obviously, this contradicts the premise of Eq (2) that the transformation of shape occurs around time t_0. However, the errors caused by this inconsistency are likely small for two reasons. First, both the time dependence of the driving force before elongation and t_{begin} are essentially independent of initial shape. Indeed, according to Figure 3, the cylindrical and head–neck invaginations, simulated with the same $f_{resist}(t)$, begin to elongate at approximately the same time, suggesting that during the time before the elongation, $f_{drive}(t)$ is similar for all shapes. Simulations of invaginations with different r_{neck}/R_{head} and $f_{resist}(t)$, described in the next section, also show that the pre-elongation $f_{drive}(t)$ are virtually independent of shape (see Figure 4A). This gives us leeway in defining shapes during the time before the elongation. Second, by using at $t < t_{begin}$ a fixed head–neck shape with the head and neck radii that would arise from shape transformation, we capture a makeup of the driving force in terms of active and viscous components at $t = t_{begin}$. Unlike the total driving force, the pre-elongation active and viscous components significantly depend on shape, and the composition of $f_{drive}(t)$ at $= t_{begin}$ in terms of these components defines the behavior of the driving force during elongation and, ultimately, the characteristics of motility of the invagination.

The head–neck invaginations elongate faster and to greater depths under higher turgor pressures

One might assume that elongation would be fastest if the resistive force were fixed at a low value. However, simulations of a head–neck invagination moving against a constant resistive force of 28.3 pN yielded average elongation rates of only ~15 nm/s (Table 1) in spite of resistance two orders of magnitude lower than experienced by a cylindrical invagination under a turgor pressure of 10 atm.

This counterintuitive behavior arises because the driving force overcomes the resistance early during patch formation. At this point, the actin flow is slow and the viscous component dominates the driving force, resulting in slow elongation. When the active component subsequently grows stronger, the viscous component decreases and even becomes resistive.These factors keep the overall driving force down, yielding relatively slow rates during the entire elongation. Conversely, a stronger and longer lasting initial resistance gives the driving force a chance to build up and may produce faster elongation rates and deeper invaginations once the driving force overcomes the resistance.

To test this prediction, we compared simulations with lower turgor pressure representative of budding yeast and the other with high turgor pressures characteristic of fission yeast. We also varied the invagination mobility coefficient μ and the parameter t_0 approximating the timing of shape change; as above, t_0 was offset by –20 s. In all simulations, the neck–head ratio was $r_{neck}/R_{head} = 0.1$ and the duration of shape change was $\tau = 0.33$ s. Table 2 summarizes the simulation parameters and results including: the duration of elongation computed as $t_{scission} - t_{begin}$ with $t_{scission}$ intepreted as the time

	Average elongation rate, nm/s		
Mobility coefficient, nm/s/pN	**Two rings of NPFs: one fixed at the base, the other moving with invagination**	**One ring of NPFs fixed on invagination at the base**	**One ring of NPFs on flat cell membrane surrounding the invagination opening (as in Mund *et al.*, 2018)**
0.01	8.1	7.3	—
0.04	12.6	13.6	—
0.08	14.3	16.6	13.2

TABLE 1: Average rates of elongation of a head–neck invagination ($r_{neck}/R_{head} = 0.1$; $R_{head} = 30$ nm) against resistive force of 28.3 pN with three invagination mobility coefficients and different arrangements of NPFs.

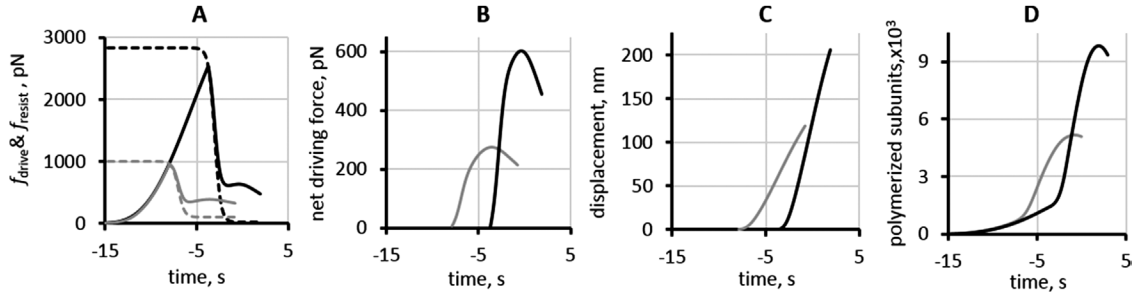

FIGURE 4: Output of simulations of models using optimized parameters for budding yeast (gray curves) and fission yeast (black curves). (A) Solid curves are f_{drive} (t); dashed curves are graphs of f_{resist} (t), see Eq (2*); (B) net forces f_{net} (t) = f_{drive} (t) – f_{resist} (t), with f_{drive} (t) and f_{resist} (t) from (A); (C) displacements; (D) polymerized actin, with the maxima of 9826 subunits in fission yeast and 5165 subunits in budding yeast. The budding yeast results are from the simulation with r_{neck}/R_{head} = 1/3. Values of t_0 used in the simulations (Table 3) are "near-saturation" as evident from graphs in A. Simulated displacements (C) and elongations rates (Table 4) are in reasonable quantitative agreement with the experimental data in Sun *et al.* (2019). Results for polymerized actin in (D) predict that at scission, actin patches in budding yeast have fewer polymerized actin subunits than in fission yeast (see discussion in *The model predicts that the peak numbers of actin are lower in budding yeast than fission yeast*).

of the peak of actin, the maximum displacement defined as the displacements at $t = t_{scission}$, the average elongation rate (the ratio of the maximum displacement and the corresponding duration of elongation), and the peak amount of polymerized actin computed as described in the Figure 2 legend.

As predicted, the simulated elongation rates were faster and the displacements longer at higher turgor pressures. Also, the timing of the resistance reduction t_0 correlated positively with elongation rates (see simulations 2 and 3) and the simulation outcomes were only modestly sensitive to μ, consistent with results in Figure 3, B and C. While both P and t_0 influence the motility of invaginations (Table 2), the impact of P is overarching because turgor pressure limits the effect of t_0 on both t_{begin} and f_{drive} (t) at t > t_{begin}. Indeed, both $f_{drive}(t_{begin})$ and t_{begin} saturate with increasing t_0 at the values controlled by turgor pressure, $\pi R_{head}^2 P$ and $f_{drive}^{-1}\left(\pi R_{head}^2 P\right)$, respectively [$f_{drive}^{-1}$ stands for the inverse function of f_{drive} (t)]. This is because the time t_{begin} is the solution of f_{drive} (t) = $f_{resist}(t)$ and f_{resist} (t) ≤ $\pi R_{head}^2 P$ [Eq (2)]; note also that $f_{drive}(t_{begin})$ is the absolute maximum of f_{drive} (t) (Figures 1, C and D, and 3, A and C). The saturation begins at $t_0 \approx f_{drive}^{-1}\left(0.8\pi R_{head}^2 P\right) + 1.3\tau$, for which $f_{resist}\left(t_{begin}\right) \approx 0.8\pi R_{head}^2 P$ (see the Supplemental Material). Interestingly, the "near-saturation" values of t_0 used in simulations 1, 2, and 6–9 (Table 2) resulted in longer elongations at lower turgor pressures, which is consistent with results in Figure 3 of Sun *et al.* (2019).

The simulation results in Table 2 agree qualitatively with the observations that invaginations in budding yeast move slower and are shorter than in fission yeast (Sun *et al.*, 2019), which is consistent with the different turgor pressures explaining these differences in the two species. Quantitatively, though, our simulations significantly overestimated the displacements in budding yeast. Note also that the elongation rates in simulations 3 and 9 are similar to those in budding and fission yeast, but they were obtained with the fourfold difference of the invagination mobility in the two yeasts, which may not be realistic.

We ran additional simulations with varying model parameters to find better agreement with reported data. Simulations with parameter sets termed "optimized" (Table 3) yielded results more consistent with the measurements by Sun *et al.* (2019) (Table 4). In these sets, mobility coefficients μ and durations of resistance reduction τ are similar for both yeasts. Parameters that differ include turgor pressure P, pressure-dependent "near-saturation" values of t_0, and neck–head ratios r_{neck}/R_{head} (recall that all simulations in Table 2

	Simulations	Simulation parameters			Simulation results				
		Turgor pressure (P), atm	Timing of resistance descent (t_0), s	Mobility coefficient (μ), nm/(s·pN)	Duration of elongation, s	Maximum displacement, nm	Average elongation rate, nm/s	Maximum elongation rate, nm/s	Maximum number of patch actin subunits, ×10³
Lower turgor pressure	1	5	–6	0.08	5.8	185	32.0	39.3	7.3
	2	3.5	–7	0.08	6.2	176	28.4	34.8	6.2
	3	3.5	–8.5	0.08	7.5	185	24.6	29.7	5.2
	4	3.5	–8.5	0.16	7.1	197	27.8	33.4	5.4
	5	3.5	–8.5	0.32	6.7	200	29.8	35.8	5.5
Higher turgor pressure	6	9	–4	0.08	5.2	202	38.8	46.8	9.4
	7	9	–4	0.16	5.1	222	43.5	52.9	10.2
	8	9	–4	0.32	5.1	236	46.8	56.7	10.6
	9	10	–3	0.32	5.0	237	47.7	59.0	11.2

TABLE 2: Parameters and results of simulations with varying P, t_0, and μ.

Parameters	Fission yeast	Budding yeast	
μ, nm/(s·pN)		0.08	
τ, s		0.33	
P, atm	10	3.5	
t_0, s	–3.0	–7.0	
r_{neck}/R_{head}	1/10	1/5	1/3

TABLE 3: Optimized parameter sets for simulating invagination motility in fission and budding yeast.

were run with the same $r_{neck}/R_{head} = 0.1$). The shapes of the invaginations may differ in the two species because of different normal forces or rigidities of the protein coat, or both. The coat rigidities are unknown, but the compressing force might be weaker in budding yeast because of lower turgor pressure, which contributes to squeezing the invagination neck, so the invaginations in budding yeast would likely have larger ratios r_{neck}/R_{head}. We solved the model for budding yeast with two values of r_{neck}/R_{head}. Simulations with $r_{neck}/R_{head} = 1/5$ ($r_{neck} = 6$ nm) yielded elongation rates closer to the observations, whereas simulations with $r_{neck}/R_{head} = 1/3$ ($r_{neck} = 10$ nm) better approximated the observed displacements (Table 4).

We introduced additional minor changes to simulations run with optimized parameters, aimed at improving the overall consistency of the model and the agreement of the simulation results with experimental observations. We replaced Eq (2) with a more accurate version of $f_{resist}(t)$ that after the invagination changes shape does not drop to zero but rather approaches $\pi P r_{neck}^2$,

$$f_{resist}(t) = \pi P R_{head}^2 \left(\frac{1-(r_{neck}/R_{head})^2}{1+e^{\frac{t-t_0}{\tau}}} + (r_{neck}/R_{head})^2 \right) \qquad (2^*)$$

In determining durations of elongation and average elongation rates, we took into account that immediately after t_{begin}, the invaginations elongate much slower than during the ensuing near-linear increase in displacement (see Figures 1D and 2C). Similar to the experimental study (Sun *et al.*, 2019), we evaluated the elongation durations and rates for the fast near-linear increase of displacements, starting at the inflection point and ending when polymerized actin reaches its maximum. The inflection points of the displacement time dependencies for the budding yeast invaginations were –6.9 s with $r_{neck}/R_{head} = 1/5$ and –6.8 s with $r_{neck}/R_{head} = 1/3$ and –2.8 s for fission yeast with $r_{neck}/R_{head} = 0.1$. The corresponding end times were –1.2 s, –0.8 s, and 1.9 s.

Figure 4 compares results for budding and fission yeast obtained with the optimized parameter sets. Graphs in panels A and B illustrate how turgor pressure affects $f_{drive}(t)$ and $f_{net}(t) = f_{drive}(t) - f_{resist}(t)$. In panel A the dashed curves are $f_{resist}(t)$ described by Eq (2*) with the maximum resistance $\pi R_{head}^2 P$ controlled by turgor pressure and thus is lower in budding yeast.

Consequently, in budding yeast elongation begins earlier during patch assembly and requires a weaker driving force, yielding lower f_{net} (panel B), slower elongation, and shorter displacements (panel C).

Simulation results obtained with optimized parameter sets agree reasonably well with the experimental data of Sun *et al.* (2019) (Table 4). The comparison reinforces the conclusion that different turgor pressures in the two yeast species are a major determinant in the observed differences of elongation rates and depths of their endocytic invaginations.

The model predicts that the peak numbers of actin are lower in budding yeast than fission yeast

Feedback between kinematics of the invagination and the accumulation of actin around the invagination explains why simulations of the model produce more polymerized actin in patches assembling under higher turgor pressures (Table 2; Figure 4D) in spite of using a fixed set of kinetic parameters for actin nucleation, polymerization, and severing (Berro *et al.*, 2010; Nickaeen *et al.*, 2019). Indeed, the amounts of actin polymerizing in patches under different turgor pressures are similar until the invaginations begin to move (Figure 4D) when the rate of polymerization and elongation increases abruptly (Figure 2, B and D).

The velocities of actin filaments (and of active Arp2/3) in the immediate vicinity of a stationary initial invagination are close to zero (due to the no-slip condition reflecting the binding of actin filaments to the coat proteins), so actin dendritic nucleation is confined to a limited space around the invagination neck (Figure 2A, left), and as the density of actin filaments increases over time, polymerization slows due to excluded volume effects. Once the invagination starts to move, its elongation speed and consequently the velocities of the filament network in the vicinity of the invagination increase sharply, as evident from the time dependences of net driving force (Figure 4B) [recall that according to Eq (1), $u(t) \propto f_{net}(t)$]. As a result, the space where new filaments can nucleate and grow expands as well. Therefore, the rate with which the invagination elongates influences the rate of actin accumulation in the patch, which is cumulatively reflected in the peak amounts of polymerized actin (Table 2).

The peak amounts of actin in endocytic patches estimated with traces of GFP-actin are ~4100–7500 subunits for fission yeast (Sirotkin *et al.*, 2010; Arasada and Pollard, 2011) and ~3600 subunits for budding yeast (Manenschijn *et al.*, 2019). The maximum numbers of actin in patches are higher in the simulations than the experimental values for both yeasts, but the ratios are roughly similar: the optimized fission yeast parameters yielded the maximum of 9829 polymerized subunits, whereas simulations of budding yeast produced maxima of 5637 subunits with $r_{neck}/R_{head} = 1/5$ and 5165 subunits with $r_{neck}/R_{head} = 1/3$. We obtained these numbers from simulation

	Fission yeast		Budding yeast		
Simulation outputs	Theory, $P = 10$ atm $r_{neck}/R_{head} = 0.1$	Experiment	Theory, $P = 3.5$ atm $r_{neck}/R_{head} = 0.2$	Theory, $P = 3.5$ atm $r_{neck}/R_{head} = 1/3$	Experiment
Duration of elongation, s	4.7	4.0–5.0	5.7	6.0	4.0–5.0
Maximum displacement, nm	205	~200	141	119	125
Average elongation rate, nm/s	43.7	51.8	24.8	19.8	23.8
Maximum elongation rate, nm/s	48.1		27.6	21.9	

TABLE 4: Comparison of simulation outcomes of models with optimized parameter sets with experimental data of Sun *et al.* (2019).

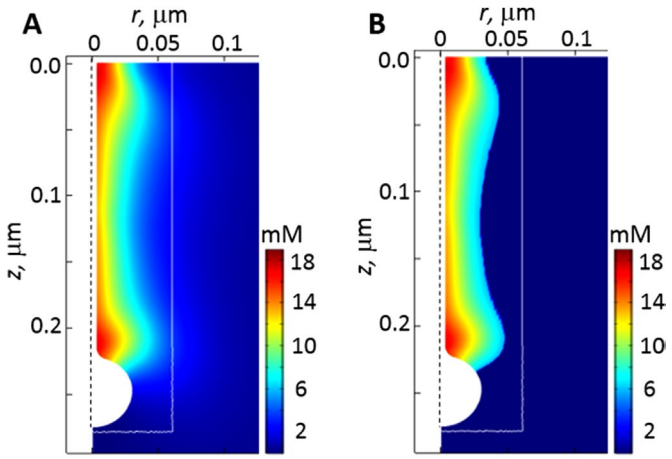

FIGURE 5: Deriving the number of actin subunits in patches from simulated actin densities. We determined the number of actin subunits in a patch by integrating actin densities within a cylinder outlined in white, which elongates with the invagination (see Figure 2 legend). (A) Snapshot of actin densities (pseudocolors) at the time of peak actin ($t = 1.9$ s), obtained with optimized parameters for fission yeast (Table 3). (B) Actin densities from A exceeding 6 mM: thresholding eliminates contributions from light-blue subspaces inside the box that may not be detected experimentally. (Vertical dashed lines represent the axis of symmetry of model geometry.)

results by integrating actin densities inside an elongating cylindrical surface that encompasses the high-density filament meshwork of the patch. The white rectangular box in Figure 5 represents a cross-section of this surface.

Figure 5A is a snapshot of the actin density distribution at the time of maximum patch actin in fission yeast ($t = 1.9$ s) obtained with optimized parameters (Table 3). Note that the white box includes light-blue spaces with relatively low densities of actin filaments, which may not be detected experimentally. Contributions from such spaces can be eliminated by imposing a density threshold. Figure 5B shows a patch of filament meshwork with densities exceeding 6 mM. Such thresholding lowers the number of subunits from 9829 to 5469 subunits, in the range of the experimental estimates for fission yeast. Importantly, applying the same threshold to simulation results obtained with the budding yeast parameters (Table 3) yielded a near proportionate decrease of the patch subunit count from 5637 to 2591 subunits for $r_{neck}/R_{head} = {}^1/_5$ and from 5165 to 2489 subunits for $r_{neck}/R_{head} = {}^1/_3$, thus maintaining the approximately twofold ratio of the numbers of subunits in the patches of the two yeasts.

The differences between the experimental estimates and simulated numbers of polymerized subunits may also reflect a modest bias against the incorporation of GFP-actin into filaments.

DISCUSSION

Sun *et al.* (2019) recorded endocytic events in budding and fission yeast in the same microscope field. The side-by-side comparison revealed remarkable similarities of the abundance of proteins at sites of endocytosis in the two yeasts, yet endocytic invaginations elongated twice as fast to twofold greater depths in fission yeast than budding yeast (Sun *et al.*, 2019). In this study, we show that a molecularly explicit model of forces exerted by actin filaments on endocytic invaginations (Nickaeen *et al.*, 2019) explains these differences. Counterintuitively, higher turgor pressures favor faster, deeper membrane invaginations using the same parameters of actin nucleation and polymerization.

At the core of our theory is an observation that polymerization of a dense network of actin filaments around an endocytic invagination not only produces a driving force parallel to the axis of invagination but also exerts orthogonal forces that compress the base of the invagination and stretch its middle. If sufficiently strong, these forces deform the nascent, cylindrical invagination into a flasklike shape as observed in electron micrographs of invaginations in budding yeast (Kukulski *et al.*, 2012; Buser and Drubin, 2013). The estimates of orthogonal forces exerted by actin at the invagination base (Nickaeen *et al.*, 2019) amount to an extra squeezing pressure with the maximum of ~8.5 atm, transforming the invagination shape from cylindrical to flasklike. Interestingly, the flask shapes, also predicted by the models of a membrane pulled under high turgor pressure by a point force at its tip (Dmitrieff and Nédélec, 2015; Ma and Berro, 2021), had wider necks than in electron micrographs. The orthogonal forces exerted by actin at the base of invagination could help narrow the neck.

The shape change, in turn, affects the driving and resistive forces. Since turgor pressure is isotropic, its resistance declines during the transition to a head–neck shape (Nickaeen *et al.*, 2019). We find that this transition also changes composition of the driving force in terms of viscous and active components due to active stresses that the polymerization of the actin filament network produces on the upper side of the invagination head. Once the driving force overcomes the declining resistive force and the invagination begins to elongate, the active component of the driving force becomes dominant and produces faster elongations and deeper invaginations (Figure 3).

Further, we find that higher turgor pressure favors faster elongations and longer displacements. For higher turgor pressure, the driving force has a chance to grow before it matches higher initial resistance. This results in higher net driving force during elongation as the resistive force drops. Thus the difference of turgor pressure in the two yeasts is a plausible explanation for the observed differences in motility characteristics of their endocytic invaginations.

The model also predicts, in qualitative agreement with experimental data on actin accumulation in endocytic patches (Sirotkin *et al.*, 2010; Arasada and Pollard, 2011; Manenschijn *et al.*, 2019), that the peak amounts of actin in the patches must be lower in budding yeast than in fission yeast because of feedback between the elongation rate and the rate of actin accumulation. Another prediction is that the ratio r_{neck}/R_{head} of the invaginations is lower in budding yeast than in fission yeast.

The modeling in this study employs certain simplifications. We describe actin filament meshwork continuously in terms of concentrations of proteins participating in actin assembly without resolving individual filaments. Given the large numbers of polymerized subunits in the patch, this approach yields reasonably accurate results while avoiding logistical burdens of discrete stochastic simulations. In this approximation, the concentration of barbed ends serves as an estimate for the local filament density, and the ratio of the density of polymerized subunits to barbed ends estimates the local average number of subunits per filament.

Our model does not include membrane mechanics and, therefore we do not solve for shape dynamics. We model elongation of a head–neck invagination by increasing the length of its neck at a rate governed by Eq (1) without changing the predefined radii of the head or neck. Parameters associated with the shape of the invagination, such as the ratio of radii r_{neck}/R_{head} and the time t_0 around which shape change takes place, are constrained by available experimental data. A more rigorous approach, based on mechanics of moving membranes (Powers, 2010), would yield the dynamic

geometry of the invagination along with the distributions of velocities and densities of polymerized actin. Of note, solving a free boundary model of invaginations elongating in a visco-active environment is significantly more involved than the determination of shapes of static invaginations, which was carried out in Dmitrieff and Nédélec (2015), Zhang *et al*. (2015), and Ma and Berro (2021). Notwithstanding the challenges, formulating and solving such a model will be possible once detailed knowledge is available on the composition and rheological properties of the endocytic membrane and its protein coat.

Even with its simplifications, our model reproduced experimentally observed elongation rates and displacements of endocytic invaginations in fission and budding yeast and uncovered the connection between turgor pressure and motility of endocytic invaginations in yeast.

METHODS

Request a protocol through *Bio-protocol*.

The coupled system of the reaction-transport equations [Eqs (S1), (S1*), and (S1**)], force-balance equation [Eq (S2)], and Eq (1) was solved using a moving-mesh solver of COMSOL Multiphysics, a software package for solving spatial multiphysics problems on finite element meshes (COMSOL Multiphysics, 2015). Because the invaginations were modeled as axially symmetric, computations were simplified by reducing the original three-dimensional (3D) problem to an equivalent 2D model formulated in (*r, z*) coordinates. Mathematical details of the model and its numerical solution are discussed in the Supplemental Material [Eqs (S1)–(S4)]. More details about the model and its numerical solution can be found in the supplemental material of (Nickaeen *et al.*, 2019).

The supplemental COMSOL simulation file, Figure2.mph, includes all details of the model implementation with parameters yielding the results of Figure 2. Using this file, one can reproduce other results reported in this study by running it in the COMSOL Multiphysics environment with accordingly modified parameters.

ACKNOWLEDGMENTS

Research reported in this publication was supported by the National Institute of General Medical Sciences of the National Institutes of Health (NIH) under award numbers R01GM026338, P41GM103313, and R01GM115636, and by the National Science Foundation (NSF) under award number MCB171605. The content is solely the responsibility of the authors and does not necessarily represent the official views of the NIH or the NSF. B.M.S. thanks Leslie Loew for continuing support. The research presented in this paper was supported by the systems, services, and capabilities provided by the University of Connecticut High Performance Computing (HPC) facility.

REFERENCES

Aghamohammadzadeh S, Ayscough KR (2009). Differential requirements for actin during yeast and mammalian endocytosis. Nat Cell Biol 11, 1039–1042.

Arasada R, Pollard TD (2011). Distinct roles for F-BAR proteins Cdc15p and Bzz1p in actin polymerization at sites of endocytosis in fission yeast. Curr Biol 21, 1450–1459.

Arasada R, Sayyad WA, Berro J, Pollard TD (2018). High-speed superresolution imaging of the proteins in fission yeast clathrin-mediated endocytic actin patches. Mol Biol Cell 29, 295–303.

Basu R, Munteanu EL, Chang F (2014). Role of turgor pressure in endocytosis in fission yeast. Mol Biol Cell 25, 679–687.

Berro J, Sirotkin V, Pollard TD (2010). Mathematical modeling of endocytic actin patch kinetics in fission yeast: disassembly requires release of actin filament fragments. Mol Biol Cell 21, 2905–2915.

Buser C, Drubin DG (2013). Ultrastructural imaging of endocytic sites in *Saccharomycescerevisiae* by transmission electron microscopy and immunolabeling. Microsc Microanal 19, 381–392.

Carlsson AE (2018). Membrane bending by actin polymerization. Curr Opin Cell Biol 50, 1–7.

Carlsson AE, Bayly PV (2014). Force generation by endocytic actin patches in budding yeast. Biophys J 106, 1596–1606.

COMSOL Multiphysics (2015). Version 5.2 [software]. Stockholm, Sweden: COMSOL AB. Available from: www.comsol.com.

de Maranon IM, Marechal PA, Gervais P (1996). Passive response of *Saccharomycescerevisiae* to osmotic shifts: cell volume variations depending on the physiological state. Biochem Biophys Res Commun 227, 519–523.

Dmitrieff S, Nédélec F (2015). Membrane mechanics of endocytosis in cells with turgor. PLoS Comput Biol 11, e1004538.

Gardel ML, Valentine MT, Crocker JC, Bausch AR, Weitz DA (2003). Microrheology of entangled F-actin solutions. Phys Rev Lett 91, 158302.

Kaksonen M, Roux A (2018). Mechanisms of clathrin-mediated endocytosis. Nat Rev Mol Cell Biol 19, 313–326.

Kasza KE, Broedersz CP, Koenderink GH, Lin YC, Messner W, Millman EA, Nakamura F, Stossel TP, MacKintosh FC, Weitz DA (2010). Actin filament length tunes elasticity of flexibly cross-linked actin networks. Biophys J 99, 1091–1100.

Kruse K, Joanny J-F, Jülicher F, Prost J, Sekimoto K (2005). Generic theory of active polar gels: a paradigm for cytoskeletal dynamics. Eur Phys J E 16, 5–16.

Kukulski W, Schorb M, Kaksonen M, Briggs JA (2012). Plasma membrane reshaping during endocytosis is revealed by time-resolved electron tomography. Cell 150, 508–520.

Lacy MM, Ma R, Ravindra NG, Berro J (2018). Molecular mechanisms of force production in clathrin-mediated endocytosis FEBS Lett592, 3586–3605.

Ma R, Berro J (2021). Endocytosis against high turgor pressure is made easier by partial coating and freely rotating base. Biophys J 120, 1625–1640.

Manenschijn HE, Picco A, Mund M, Rivier-Cordey AS, Ries J, Kaksonen M (2019). Type-I myosins promote actin polymerization to drive membrane bending in endocytosis. eLife 8, e44215.

Mullins RD, Kelleher JF, Xu J, Pollard TD (1998). Arp2/3 Complex from *Acanthamoeba* binds profilin and cross-links actin filaments. Mol Biol Cell 9, 841–852.

Mund M, van der Beek JA, Deschamps J, Dmitrieff S, Hoess P, Monster J-L, Picco A, Nédélec F, Kaksonen M, Ries J (2018). Systematic nanoscale analysis of endocytosis links efficient vesicle formation to patterned actin nucleation. Cell 174, 884–896.

Nickaeen M, Berro J, Pollard TD, Slepchenko BM (2019). Actin assembly produces sufficient forces for endocytosis in yeast. Mol Biol Cell 30, 2014–2024.

Powers TR (2010). Dynamics of filaments and membranes in a viscous fluid. Rev Mod Phys 82, 1607–1631.

Prost J, Jülicher F, Joanny J-F (2015). Active gel physics. Nat Phys 11, 111–117.

Schaber J, Adrover MA, Eriksson E, Pelet S, Petelenz-Kurdziel E, Klein D, Posas F, Goksör M, Peter M, Hohmann S, Klipp E (2010). Biophysical properties of *Saccharomycescerevisiae* and their relationship with HOG pathway activation. Eur Biophys J 39, 1547–1556.

Scher-Zagier JK, Carlsson AE (2016). Local turgor pressure reduction via channel clustering. Biophys J 111, 2747–2756.

Sirotkin V, Berro J, Macmillan K, Zhao L, Pollard TD (2010). Quantitative analysis of the mechanism of Endocytic actin patch assembly and disassembly in fission yeast. Mol Biol Cell 21, 2894–2904.

Sun Y, Schönenberg J, Chen X, Jiang T, Kaplan C, Xu K, Pollard TD, Drubin DG (2019). Direct comparison of clathrin-mediated endocytosis in budding and fission yeast reveals conserved and evolvable features. eLife 8, e50749.

Tseng Y, Wirtz D (2004). Dendritic branching and homogenization of actin networks mediated by Arp2/3 complex. Phys Rev Lett 93, 258104.

Zhang T, Sknepnek R, Bowick M, Schwarz J (2015). On the modeling of endocytosis in yeast. Biophys J 108, 508–519.